Quantum Energy Extraction: Fundamental Limits and Practical Models

Daniel S. Zachary

Advanced Academic Program, Krieger School of Arts and Sciences, Johns Hopkins University, Washington DC, 555 Pennsylvania Avenue, NW, 20001, USA

E-mail: d.s.zachary@jhu.edu

29 August 2025

Abstract. We propose the Quantum Uncertainty-Informed Networked Teleportation protocol, or QUINT, a framework for extracting energy from quantum vacuum fluctuations by exploiting spatially-structured entanglement. Extending conventional quantum energy teleportation (QET) protocols, QUINT protocol hypothesizes that entanglement correlations may be geometrically organized, inspired by the ER=EPR conjecture (treated here as a heuristic for structured entanglement). This structure enables enhanced energy extraction and directional sensitivity across a network of QET nodes. We present the formalism for per-cycle energy extraction, including constraints imposed by quantum energy inequalities, and introduce a simple dynamical model for entanglement depletion and recovery. Observable signatures of the protocol include localized stress-energy redistributions, phase shifts, and anisotropies in extraction efficiency. Our framework provides a pathway to probe structured vacuum entanglement and suggests experimentally testable predictions for quantum-optical or field-theoretic systems. By focusing on measurable energy flows rather than speculative geometries, the QUINT protocol establishes a novel approach to quantum energy engineering and lays the groundwork for exploring the operational consequences of vacuum entanglement networks.

Keywords: quantum energy teleportation, vacuum energy extraction, negative energy, Casimir effect, quantum metrology, semiclassical gravity, spacetime curvature, quantum entanglement networks

I. Introduction and motivation

Quantum fields in the vacuum state exhibit nontrivial fluctuations that can be harnessed using quantum energy teleportation (QET) protocols [14, 18]. In these protocols, local measurements on one region of the field allow a distant region to extract energy without direct energy transport. While standard QET treats the vacuum as a uniformly entangled Gaussian state, recent developments suggest that entanglement may possess a geometric structure, as hypothesized by the ER=EPR conjecture [26, 25]. If spatially separated regions are connected via microscopic Einstein-Rosen bridges, vacuum fluctuations acquire an effective geometric and energetic organization, potentially enhancing energy extraction. The QUINT protocol (Quantum Uncertainty-Informed Networked Teleportation) builds upon this idea, aiming to define operational rules and per-cycle energy extraction limits for a networked system of QET nodes while respecting quantum energy inequalities (QEIs) [9, 13].

II. The QUINT Protocol: Quantum Uncertainty-Informed Networked Teleportation

HEREIAM

The QUINT protocol extends conventional quantum energy teleportation (QET) [15, 16] by exploiting spatially-structured entanglement across a network of localized nodes. In standard QET, energy is teleported from a measurement region (Alice) to a distant extraction region (Bob) via vacuum correlations, without classical energy flow. In QUINT, this procedure is organized into a continuous operational framework in which each Alice–Bob node pair functions as an energy extraction unit sensitive to networked entanglement.

In a single cycle, Alice performs a local measurement on a field observable, such as the scalar field amplitude or a quadrature operator, collapsing the entangled vacuum state in her region and injecting positive energy $\delta E_A > 0$. The outcome of this measurement, labeled m, is transmitted to Bob through a classical channel, conveying information but not energy. Upon receiving the outcome, Bob implements a conditional local unitary operation $U_B(m)$ designed to extract energy from the vacuum in his region. The optimal energy extracted for a given outcome is

$$\delta E_B^*(m) = -\frac{C_m^2}{2\,\chi_B}, \tag{1}$$

where C_m is the connected correlator induced by Alice's measurement, and χ_B is Bob's local susceptibility. Averaging over all outcomes yields

$$E_{\text{out}} = \sum_m p_m\, \delta E_B^*(m), \tag{2}$$

with p_m the probability of observing outcome m. If correlations between Alice and Bob's regions vanish ($C_m \to 0$), energy extraction is suppressed.

To scale the energy extraction process, multiple A–B pairs can be arranged into a *QUINT array*, a network of entanglement-sensitive nodes [6]. Spatial correlations across the array allow directional sensitivity to entanglement gradients and coherent reinforcement of extraction along

structured pathways. This arrangement also provides a method to probe anisotropies in vacuum fluctuations. A schematic of a three-pair QUINT array is shown in Figure 1.

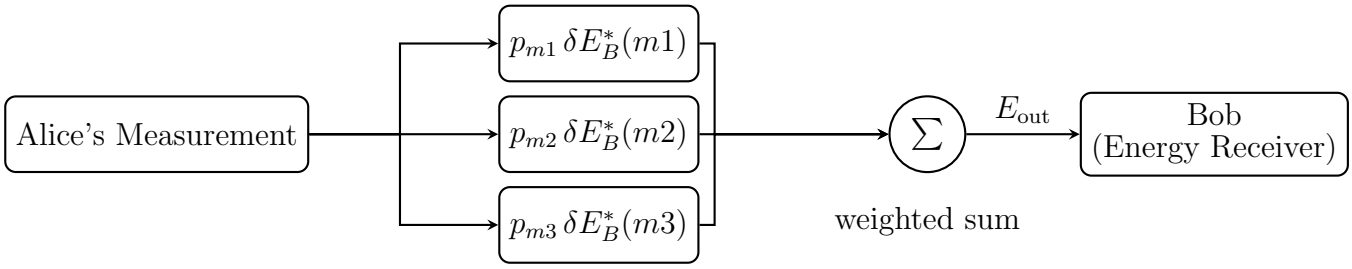

Figure 1: Compact schematic of outcome-conditioned QET energy extraction. Alice performs a measurement, each outcome m contributes in parallel with probability p_m and associated extractable energy $\delta E_B^*(m)$. The total output energy E_{out} is delivered to Bob.

Inspired by the ER=EPR conjecture [26], the effective correlator may be enhanced relative to conventional QET,

$$C_m^{\text{QUINT}} > C_m^{\text{QET}}. \tag{3}$$

This geometric structuring increases per-cycle energy extraction, allowing for directional control across the array and providing the foundation for designing quantum Carnot-like cycles that maximize sustainable power output. While these enhancements are hypothetical, they are constrained by quantum energy inequalities [9, 13], ensuring that local negative-energy densities remain bounded. In this framework, entanglement acts as a conduit for energy rearrangement without classical energy transport, highlighting the operational significance of structured vacuum correlations.

III. Quantum Carnot Cycle and Entanglement Resource Dynamics

The operational framework of QET-assisted cycles can be understood via a conceptual schematic of sequential steps, shown in Fig. 2. Each cycle involves energy injection, local measurement, classical signaling, extraction, and reset. This schematic highlights the correspondence between QET operations and a Carnot-like cycle analogy, providing intuition for resource flow and extraction limitations.

To describe the evolution of the entanglement resource during repeated cycles, we consider a discrete update model:

$$R_{n+1} = R_n - E_c + \frac{\tau - \Delta t}{\tau}\big(R_\infty - R_n\big), \tag{4}$$

where R_n is the resource available at the start of cycle n, E_c is the energy extracted per cycle, τ is the recovery timescale, and R_∞ is the asymptotic resource level (see App Appendix B for the details of the recursion relation and for the steady state details). The net work over a single cycle accounts for the energy cost of establishing entanglement:

$$W_{\text{net}} = W_{\text{QET}} - E_{\text{ent}}. \tag{5}$$

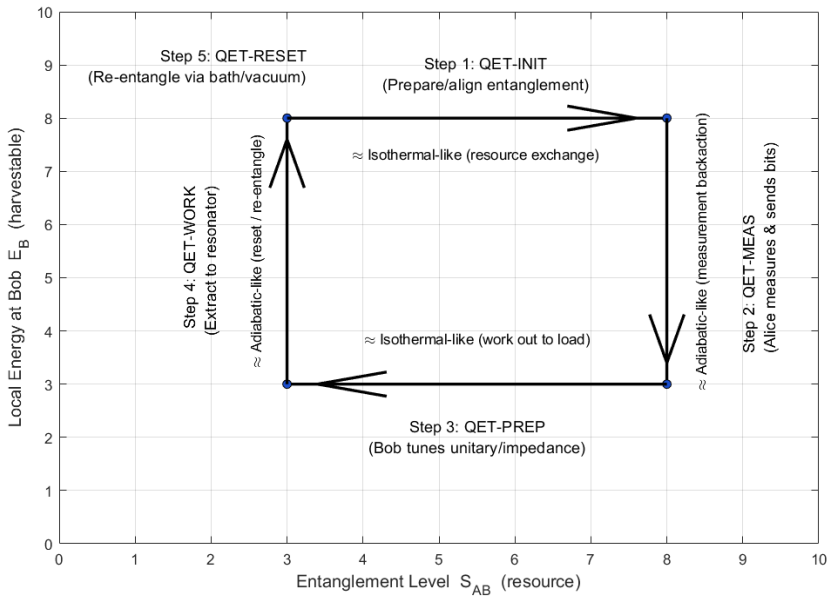

Figure 2: Schematic of a single QET-assisted (Carnot-like) cycle. The steps shown are: injection of energy into the subsystem (S1), measurement (S2), signaling to the extraction site (S3), local extraction of energy (S4), and reset of the subsystem (S5). This conceptual diagram guides understanding of the entanglement resource dynamics and provides a Carnot-like cycle analogy.

The maximum extractable power for a given cycle period T_{cycle} is then

$$P_{\max} = \frac{E_c}{T_{\text{cycle}}} \leq \frac{R_{\max}}{\gamma T_{\text{cycle}}}, \tag{6}$$

where $R_{\max}$ is the peak entanglement resource and γ is a system-dependent recovery factor.

Figure 3 presents numerical simulations consolidating the entanglement dynamics, Carnot-like QET cycle, and operational constraints. The main panel shows $R(t)$ for multiple cycle durations T_{cycle}, illustrating the interplay between extraction events and recovery. Insets display (a) descending entanglement curves from Quantum Carnot cycle simulations, and (b) maximum power $P_{\max}$ versus cycle period and extraction yield versus subsystem separation. This approach preserves conceptual clarity while incorporating all previously separate simulation data for resource recovery, power scaling, and yield.

Each cycle's net work accounts for the energy cost of establishing entanglement [10, 12], and the resource recovery dynamics are modeled following standard QET frameworks [18].

IV. Observable Signatures and Networked Quantum Energy Extraction

Building upon the entanglement resource dynamics characterized in Sec. III, we now discuss the measurable consequences of repeated QET-assisted cycles, their networked generalization, and possible experimental realizations. The formalism underlying both single-cycle and networked extraction protocols provides a unified description of how quantum correlations can

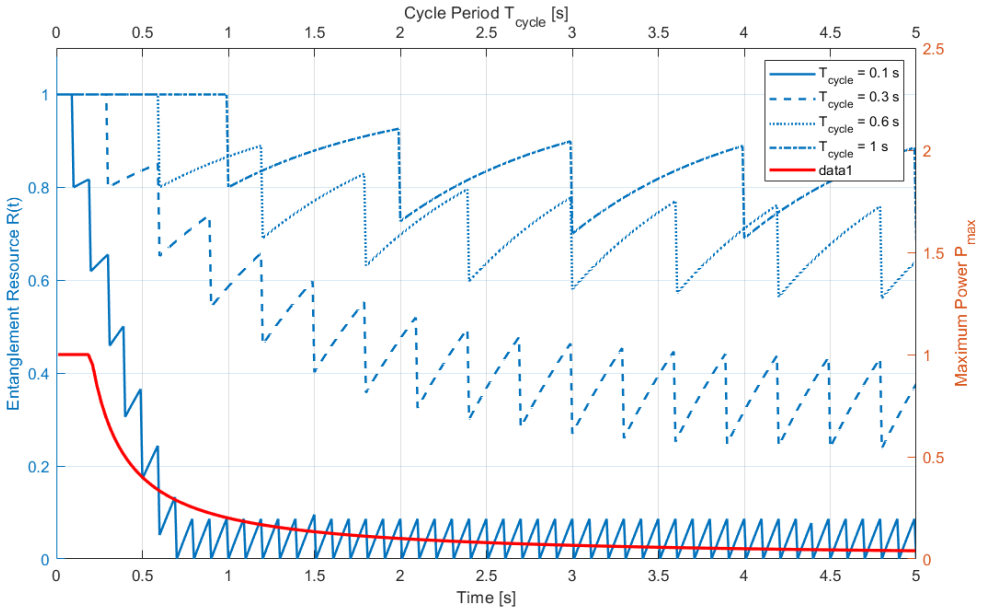

Figure 3: Entanglement resource dynamics during repeated QET-assisted cycles. The main panel depicts $R(t)$ for multiple cycle durations T_{cycle}, showing the effect of recovery time τ on resource availability. Insets display: (a) the descending $R(t)$ curves from Quantum Carnot cycle simulations for illustrative extraction sequences, and (b) maximum power $P_{\max}$ vs cycle period and extraction yield vs subsystem separation, demonstrating operational constraints for stable energy extraction. These subpanels consolidate the numerical simulations previously shown separately in RcDynamics and QuantumCarnotCycle_Simulations.

be operationalized into extractable energy, while also clarifying the observable stress-energy signatures that such processes inevitably imprint on the local vacuum.

In a single QET cycle, energy is locally injected, measured, and subsequently extracted at a spatially separated site. The per-cycle outcome-conditioned extracted energy can be formalized as [14, 18]

$$\Delta E_B^*(m) = -\frac{C_m^2}{2\,\chi_B}, \tag{7}$$

where C_m characterizes the correlation between measurement outcome m and the extraction operator, and χ_B is the susceptibility of the extraction subsystem.

The measurement at Alice's site is described by a set of *Kraus operators* $\{M_m\}$, with each M_m corresponding to a particular outcome m. These operators encode both the outcome probabilities $p_m = \langle 0|M_m^\dagger M_m|0\rangle$ and the back-action of the measurement on the quantum field. The post-measurement state for outcome m is $M_m|0\rangle$, and the operators satisfy the completeness relation $\sum_m M_m^\dagger M_m = I$.

Averaging over all outcomes yields the expected energy per cycle:

$$\langle \Delta E_B \rangle = \sum_m p_m \Delta E_B^*(m), \tag{8}$$

while the corresponding stress-energy redistribution in the field is

$$\delta\langle T_{00}(\mathbf{x})\rangle \sim \sum_m p_m \, \langle 0|M_m^\dagger \, T_{00}(\mathbf{x}) \, M_m|0\rangle - \langle 0|T_{00}(\mathbf{x})|0\rangle, \tag{9}$$

providing a local observable signature that can in principle be probed via phase shifts, local recoil, or cavity field response [10, 12].

The correlation factor C_m and the susceptibility χ_B determine the magnitude of extractable energy $\Delta E_B^*(m)$, and their flow into B highlights the role of networked coupling in QUINT arrays.

This single-pair description generalizes naturally to spatially distributed quantum networks. Each cycle proceeds through energy injection at subsystem A, local measurement to obtain outcome m, classical signaling of m to a remote site B, conditional local operations to extract energy at B, and eventual reset of A for reuse [14, 18]. In this networked setting, multiple A–B pairs form a QUINT (Quantum Uncertainty-Informed Networked Teleportation) array, enabling directional mapping of entanglement gradients and optimized energy extraction across distributed nodes. The efficiency depends on subsystem separation d, alignment of entanglement anisotropies, and the topology of the network itself. In analogy to entanglement gradient mapping [26], nodes aligned along high-correlation pathways yield enhanced extraction, while orthogonal orientations show diminished $\langle \Delta E_B \rangle$.

The expected yield across N networked nodes generalizes to

$$\langle \Delta E_{\text{net}} \rangle = \sum_{i=1}^{N} \sum_m p_i(m) \, \Delta E_{B_i}^*(m), \tag{10}$$

capturing the aggregate resource conversion across the network. Numerical MATLAB simulations of QUINT arrays, shown in Fig. 4, illustrate how extractable power depends on cycle duration, subsystem separation, and network connectivity. These results indicate that the interplay between cycle period T_{cycle}, recovery time τ, and network geometry sets upper bounds on both instantaneous power and cumulative yield [18]. This naturally raises the question of *scaling*: how the total extractable energy and power grow with network size N. Depending on the interplay between local correlations, subsystem separation, and recovery dynamics, QUINT arrays can exhibit linear, sub-linear, or even saturating scaling of $\langle \Delta E_{\text{net}} \rangle$ with N, providing insight into the optimal network design for maximum yield.

Candidate experimental platforms for realizing QET-assisted networks include superconducting qubit arrays, trapped-ion chains, and cavity-QED systems. These provide high-fidelity local control, measurement, and outcome-conditioned feedback, while Casimir cavity configurations offer the possibility of directly probing vacuum stress-energy modifications with precision force sensing [5, 22]. Each platform presents trade-offs in achievable energy per cycle, decoherence rates, and scalability, which must be optimized alongside network configuration. Table 1 offers some experimental setups.

Finally, structured entanglement patterns inspired by ER=EPR considerations may enhance extraction efficiency by concentrating correlations along operationally relevant pathways [26, 25]. Coordinated measurements and conditional operations across multiple nodes maximize resource

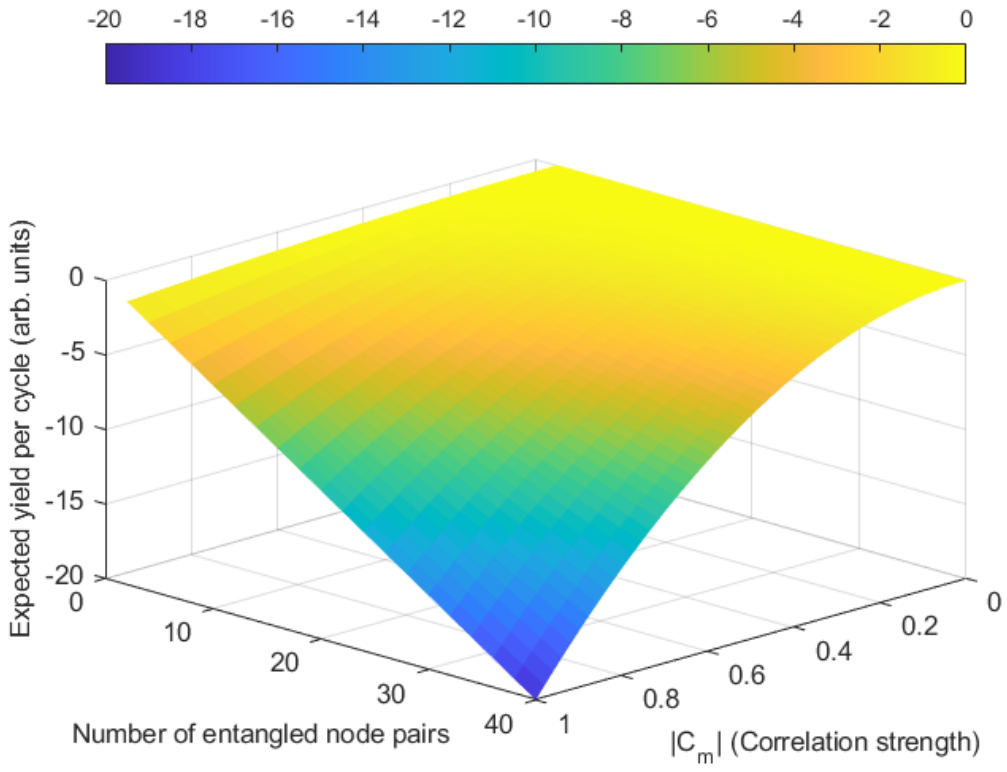

Figure 4: Simulation of a QUINT array showing the expected per-cycle yield across networked entangled nodes. The surface plot illustrates how the total extractable energy depends on the number of entangled node pairs N and the correlation strength $|C_m|$. Higher correlations and larger networks increase the yield, while the interplay between cycle period, recovery time, and network geometry (see main text) sets practical bounds on instantaneous power and cumulative energy extraction.

Platform	**Energy per cycle**	**Deco-herence**	**Scalability**	**Observable**	**Cost / Feas.**
Superconducting qubits	10^{-24}–10^{-21} J	μs–ms	Medium (chip-level)	Current/voltage	High, $\$10^6$–$10^7$
Trapped ions	10^{-25}–10^{-22} J	ms–s	Low–Med (10–100)	Fluorescence, phonons	Medium, $\$10^7$
Cavity QED	10^{-26}–10^{-23} J	μs–ms	Med–High	Photon stats, phase	High, $\$10^6$–$10^7$
Casimir cavities	10^{-27}–10^{-24} J	Stable	High (plate arrays)	Force sensing	Med–High, $\$10^6$+

Table 1: Candidate experimental platforms for QET-assisted networks. Comparison of energy scales, decoherence, scalability, observables, and practical feasibility.

utilization while maintaining subsystem coherence. Heuristic models predict that such structured networks achieve scaling of yield with both node number and connectivity, providing an

experimentally testable signature of entanglement-assisted power amplification.

V. QUINT Arrays: Networked Yield and Simulation

The basic QUINT protocol defined in Section II can be generalized to an array of entangled node pairs distributed across a spatial region. Each pair (A_i, B_i) undergoes a local measurement–operation cycle, with outcomes aggregated to yield an effective directional redistribution of stress–energy. The network configuration determines the constructive or destructive interference of negative energy densities, as well as the scalability of total extractable energy.

For a single node pair, the optimal conditional extractable energy (per outcome m) is

$$\Delta E^*_{B,i}(m) = -\frac{C^2_{m,i}}{2\chi_{B,i}}, \tag{11}$$

where $C_{m,i}$ denotes the correlation coefficient between the local measurement at node A_i and the field response at node B_i, and $\chi_{B,i}$ is the local susceptibility of the target Hamiltonian [14, 17].

Averaging over outcomes gives the per-node expected yield,

$$\langle \Delta E_{B,i} \rangle = -\sum_m p_{m,i} \frac{C^2_{m,i}}{2\chi_{B,i}}, \tag{12}$$

where $p_{m,i}$ are outcome probabilities determined by the measurement statistics at A_i.

For N entangled pairs, assuming negligible cross-talk and approximately independent operations, the leading-order network yield is additive:

$$\langle \Delta E_{\text{tot}} \rangle \approx \sum_{i=1}^{N} \langle \Delta E_{B,i} \rangle. \tag{13}$$

In more structured entanglement geometries, constructive interference of stress–energy deficits can occur, producing a network enhancement factor $\Gamma(N, d)$, where d denotes the inter-node spacing:

$$\langle \Delta E_{\text{tot}} \rangle = \Gamma(N, d) \sum_{i=1}^{N} \langle \Delta E_{B,i} \rangle, \tag{14}$$

with $\Gamma \geq 1$ for aligned arrays and $\Gamma < 1$ when destructive interference dominates. Here $\Gamma(N, d)$ captures overlap effects between spatially distributed stress–energy deficits. Constructive interference ($\Gamma > 1$) arises when induced curvature profiles reinforce one another, while destructive interference ($\Gamma < 1$) reflects partial cancellation due to out-of-phase or anti-aligned geometries. Explicit evaluation of these overlap integrals, including Bessel-function structure in continuum limits and detailed $C_{m,i}$ dependence, is deferred to the Appendix.

A. Simulation of QUINT Arrays

To explore scaling and interference effects in a simplified setting, we implemented a MATLAB simulation of networked QUINT arrays. Each node pair was modeled with randomized correlation

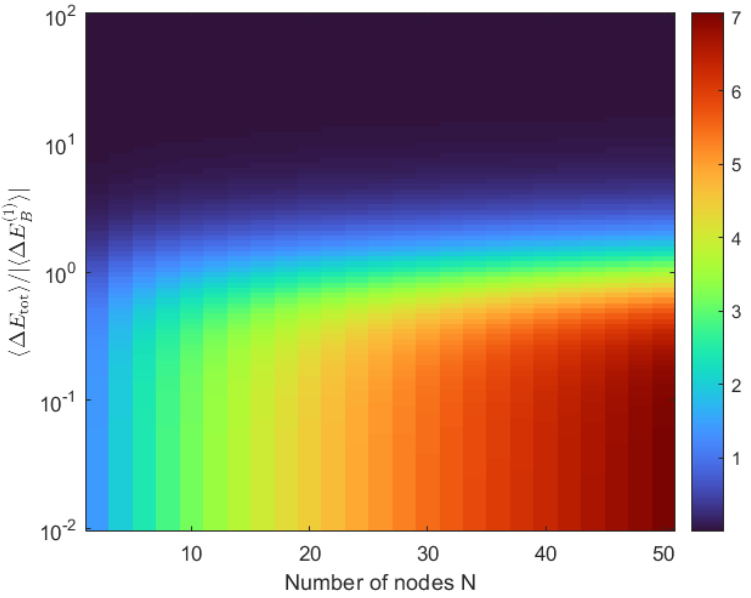

Figure 5: Simulation of QUINT-array yield versus subsystem separation d (horizontal) and node count N (vertical). Color shows the per-cycle total extractable energy normalized to the single-node expectation, $\langle \Delta E_{\rm tot} \rangle / |\langle \Delta E_B^{(1)} \rangle|$ (dimensionless). Nodal/lobed features reflect Bessel-type radial interference and angular harmonics; see Appendix C.

coefficients $C_{m,i}$ drawn from Gaussian distributions consistent with field vacuum correlations, and susceptibilities $\chi_{B,i}$ determined from cavity or circuit parameters [18, 19, 11].

The simulation sweeps both N (number of pairs) and d (node spacing), computing the enhancement factor $\Gamma(N, d)$ by comparing the networked yield (14) to the naive additive model (13). Each simulation point averages over 500 realizations of randomized $C_{m,i}$ coefficients to ensure statistical convergence.

We further evaluate the dependence of extractable energy on subsystem separation d and the number of networked nodes N. A finite relaxation time (lag) between QET cycles is assumed, representing the need for entanglement to re-establish between extractions. This lag suppresses yield at high repetition but does not alter the qualitative scaling with N and d.

As discussed in Appendix Appendix C, the nodal structure visible in Fig. 5 can be formally related to the zeros of Bessel-type mode functions arising in the continuum limit of the array.

The results (Fig. 5) indicate that Γ grows superlinearly for closely spaced nodes ($d \ll \lambda$), consistent with cooperative negative-energy redistribution. Conversely, large separations ($d \gg \lambda$) suppress enhancement, causing scaling to approach the naive additive model. These findings suggest that engineered geometries could optimize network yield for experimental implementations.

VI. Energy Extraction Limits and Quantum Carnot Cycle

A. Fundamental Bounds and Quantum Energy Inequalities

The extractable energy in a QUINT or QET protocol is fundamentally constrained by quantum energy inequalities (QEIs) and causality bounds. For a given localized operation, the maximum negative energy density $\langle T_{00}\rangle_{\min}$ is bounded, preventing arbitrary violations of the averaged null energy condition [11, 8, 14].

Without QEIs:

For an outcome-conditioned measurement at node A, the per-cycle optimal extractable energy $\Delta E_B^*(m)$ is limited by

$$\Delta E_B^*(m) \geq -\frac{C_m^2}{2\chi_B} \leq \Delta E_{\max}, \tag{15}$$

where $\Delta E_{\max}$ encodes both the QEI-imposed lower bound and operational constraints such as finite measurement strength, environmental decoherence, and Landauer erasure costs [18].

These bounds ensure causality is preserved: the spatial extent of negative energy regions and the temporal separation between injection and extraction events are tightly constrained, preventing superluminal signaling through energy teleportation channels.

B. Entanglement Resource Depletion and Recovery

The entanglement resource is represented by a normalized fraction $R(t) \in [0, 1]$ denoting the usable entanglement at time t. Under a minimal continuous-time approximation the competing effects of resource consumption during QET/QUINT cycles and re-establishment of correlations are captured by the balance equation

$$\frac{dR}{dt} = -\frac{1}{\tau_{\text{cycle}}} R(t) + \frac{1 - R(t)}{\tau_{\text{rec}}}, \tag{16}$$

where τ_{cycle} is the characteristic timescale of depletion associated with the average operation interval (or effective drain rate) and τ_{rec} is the recovery timescale for re-entanglement driven by vacuum fluctuations or ancillary operations. The depletion term $-R/\tau_{\text{cycle}}$ models consumption proportional to the presently available resource; the recovery term $(1 - R)/\tau_{\text{rec}}$ vanishes when $R = 1$ and is maximal when $R = 0$, ensuring relaxation toward a fully replenished state. Setting $\dot{R} = 0$ in Eq. (16) yields the steady-state resource fraction,

$$R_{\text{ss}} = \frac{\tau_{\text{rec}}}{\tau_{\text{cycle}} + \tau_{\text{rec}}}, \tag{17}$$

which interpolates between $R_{\text{ss}} \to 1$ for fast recovery ($\tau_{\text{rec}} \ll \tau_{\text{cycle}}$) and $R_{\text{ss}} \to 0$ for rapid cycling ($\tau_{\text{cycle}} \ll \tau_{\text{rec}}$). The linear ordinary differential equation (16) admits the closed-form transient solution,

$$R(t) = R_{\text{ss}} + \big(R(0) - R_{\text{ss}}\big) \exp\Big(-\frac{t}{\tau_{\text{eff}}}\Big), \qquad \tau_{\text{eff}} = \frac{\tau_{\text{cycle}}\, \tau_{\text{rec}}}{\tau_{\text{cycle}} + \tau_{\text{rec}}}, \tag{18}$$

so that the approach to steady state is exponential with effective time constant τ_{eff}. Physically, increasing cycle frequency (reducing τ_{cycle}) raises short-time extractable power but lowers the sustainable resource level R_{ss}, while accelerating recovery (reducing τ_{rec}) improves long-run yield. Equation (16) therefore captures the key tradeoff between high-frequency operation and entanglement replenishment that constrains continuous extractable energy in QET/QUINT protocols.

C. Maximum Power, Cycle Time, and Numerical Examples

The cycle-averaged power per node is,

$$P = \frac{\langle \Delta E_B \rangle}{T_{\text{cycle}}}, \tag{19}$$

which, combined with resource depletion dynamics, gives an effective maximum power

$$P_{\max} = \frac{R_{\text{ss}}\, \Delta E_{\max}}{T_{\text{cycle}}}. \tag{20}$$

The total extracted energy E_{tot} over n cycles satisfies

$$E_{\text{tot}} = n\, R_{\text{ss}}\, \Delta E_{\max}, \quad \text{with } n = \frac{t_{\text{op}}}{T_{\text{cycle}}}, \tag{21}$$

so that

$$E_{\text{tot}} = \frac{t_{\text{op}}}{T_{\text{cycle}}}\, R_{\text{ss}}\, \Delta E_{\max}. \tag{22}$$

allowing explicit planning of cycle time T_{cycle} to achieve a target energy extraction.

To illustrate the scaling of extractable power in QUINT or QET protocols, consider a typical cycle time of

$$T_{\text{cycle}} = 10^{-6}\,\text{s}, \tag{23}$$

which is consistent with MHz-scale operations in superconducting qubits or optical cavities. We assume a per-cycle extractable energy of

$$\langle \Delta E_B \rangle \sim 10^{-21}\,\text{J}, \tag{24}$$

and a recovery timescale

$$\tau_{\text{rec}} \sim 10^{-3}\,\text{s}. \tag{25}$$

The instantaneous power per node is then

$$P = \frac{\langle \Delta E_B \rangle}{T_{\text{cycle}}} \sim 10^{-15}\,\text{W}. \tag{26}$$

Scaling to multiple nodes, for example $N = 10^3$ pairs operating in parallel, yields

$$P_{\text{tot}} \sim 10^{-12}\,\text{W}, \tag{27}$$

while for a macroscopic network of $N = 10^{12}$ pairs, the total extracted power reaches

$$P_{\text{tot}} \sim 10^{-3}\,\text{W}, \tag{28}$$

demonstrating the leverage of networked entanglement despite extremely small per-cycle energy.

The choice of $T_{\text{cycle}} \sim 10^{-6}\,\text{s}$ is motivated by experimental constraints in superconducting qubits and cavity QED, where gate operations occur on timescales of 10^{-9}–10^{-7} s, measurements take approximately 10^{-6} s, and feedback or reset cycles are typically on the order of $1\,\mu$s. In high-finesse optical cavities, photon lifetimes are also of order 10^{-6} s, which naturally sets a lower bound on the cycle duration for storing, measuring, and re-injecting energy.

These examples illustrate that optimal power extraction requires a balance between short cycle times and sufficient entanglement recovery, highlighting practical operational limits for experimental implementations. But if one imagines an extreme, Avogadro-scale network with

$$N \sim 6 \times 10^{23} \text{ entangled pairs}, \tag{29}$$

the total instantaneous power would scale to

$$P_{\text{tot}} \sim N\,P \sim 6 \times 10^{8}\,\text{W}, \tag{30}$$

approaching a gigawatt-scale output. Maintaining coherence across such a vast number of nodes is extremely challenging due to decoherence from environmental noise, photon loss, and imperfect qubit operations. Finite cavity volumes and spatial constraints limit the density of entangled pairs that can be practically implemented, while control overhead for measurement, feedback, and synchronization scales rapidly with network size. Although advances in error correction, cavity engineering, and modular architectures may partially mitigate these issues, achieving Avogadro-scale coherent networks remains far beyond current technology. These limitations highlight the practical gap between theoretical extrapolations and experimental feasibility [4, 24, 23].

VII. Observable Signatures and Experimental Considerations

A. Local Stress-Energy Redistribution

The localized injection and extraction of energy in QUINT or QET protocols produce measurable perturbations of the stress–energy tensor, $\delta T_{00}(\vec{x}, t)$. These perturbations can be probed via phase shifts in optical or matter-wave interferometers, or via recoil effects on mechanical elements coupled to the field [18, 11].

For a single node pair, the induced perturbation is

$$\delta T_{00}(\vec{x}, t) \sim \sum_m p_m \Delta E_B^*(m) f(\vec{x} - \vec{x}_B, t - t_m), \tag{31}$$

where $f(\vec{x}, t)$ encodes the spatiotemporal profile of the energy redistribution. The signal strength scales linearly with the number of coordinated nodes in a networked array and is modulated by interference effects, as described in Sec. V.

B. Directional and Network Effects

In structured arrays, the extractable energy exhibits anisotropic redistribution patterns reflecting gradients in entanglement and measurement correlations. The directional enhancement factor $\Gamma(N, d)$ (Eq. 14) produces measurable differences in local δT_{00} along preferred axes, which can be detected via aligned interferometric probes or multi-node readout schemes.

Mapping these anisotropies provides experimental access to entanglement geometry and network coherence, offering a diagnostic tool for both protocol optimization and verification of negative-energy redistribution.

C. Potential Experimental Platforms

Several candidate platforms are available for observing QUINT-induced signatures. In quantum optics, optical cavities with squeezed states and fast homodyne detection enable high-bandwidth measurement of small energy redistributions. Superconducting circuits, including qubits and resonators, offer tunable coupling to microwave fields with single-photon sensitivity and controllable entanglement resources [18, 19]. Trapped ion chains provide motional degrees of freedom that can act as sensitive probes of local field excitations, including vacuum fluctuations. Micro- and nano-scale Casimir cavities present an opportunity to explore boundary-condition–dependent vacuum energy redistribution and QET-based extraction. Each platform presents tradeoffs in scalability, coherence time, and measurement sensitivity. Integration with multi-node arrays, as explored in Sec. V, is essential for realizing enhanced networked yield and directional observables.

Each platform presents tradeoffs in scalability, coherence time, and measurement sensitivity. Integration with multi-node arrays, as explored in Sec. V, is essential for realizing enhanced networked yield and directional observables.

VIII. Implementation Strategies and Experimental Outlook

Realizing QUINT protocols in the laboratory requires careful consideration of coherence, control, and measurement sensitivity across multiple nodes. The primary challenge is maintaining high-fidelity entanglement while performing outcome-conditioned operations at each node, particularly when networked arrays span spatially separated regions. Protocol timing, node spacing, and synchronization must be optimized to balance maximum extractable energy with entanglement recovery dynamics described in Sec. VI.

Experimental implementation can leverage state-of-the-art quantum platforms. In optical cavity systems, fast homodyne detection and dynamically tunable squeezing allow precise monitoring of field quadratures, while superconducting circuits provide strong coupling to microwave resonators with high single-photon sensitivity. Trapped ions and Casimir cavities offer alternative approaches where motional or boundary-dependent vacuum modes serve as observables. Each platform imposes specific constraints on cycle times, coherence length, and scalability, and the choice of platform determines the achievable network enhancement factor $\Gamma(N, d)$.

Scaling to multi-node arrays introduces additional considerations. Crosstalk between nodes, finite-speed signal propagation, and collective decoherence may suppress constructive interference of negative energy densities if not carefully mitigated. Numerical simulations, such as those presented in Sec. V, provide guidance for optimizing inter-node spacing and array geometry to maximize directional yield and networked enhancement.

Overall, these considerations suggest that while laboratory realization of QUINT arrays is challenging, careful integration of high-fidelity entanglement, fast measurement, and network design can make experimental observation of negative energy redistribution feasible. These strategies form the basis for planning near-term proof-of-principle demonstrations and guide longer-term efforts to scale QUINT protocols toward larger quantum networks.

IX. Conclusion and Outlook

In this work, we have extended the QUINT protocol to networked arrays of entangled node pairs and explored both theoretical limits and experimental considerations for negative energy extraction. We derived per-node and networked yields, accounting for constructive and destructive interference effects, and analyzed the role of entanglement depletion and recovery in determining maximum extractable energy and power. MATLAB-based simulations illustrate scaling behavior, highlighting the importance of array geometry and inter-node spacing in achieving enhanced network yield.

We also discussed observable signatures, including local stress–energy redistribution and directional effects, and identified candidate experimental platforms spanning optical cavities, superconducting circuits, trapped ions, and Casimir cavities. Each platform presents tradeoffs in sensitivity, coherence time, and scalability, and careful integration of multi-node arrays is essential to realize directional enhancements predicted by the theory.

Looking forward, the results provide a roadmap for near-term proof-of-principle experiments and inform strategies for scaling QUINT protocols to larger quantum networks. Future work may explore optimized network geometries, error mitigation strategies, and hybrid platforms that combine complementary measurement and control capabilities. These studies will advance our understanding of quantum energy transport and its potential experimental realization, bridging fundamental theory with laboratory implementation.

Appendix A. Modeling Local Stress–Energy Extraction

The implementation of a quantum energy teleportation (QET) protocol requires a concrete model for the extraction of local stress–energy from the vacuum. In this appendix we summarize the Gaussian modeling framework used in Section IV, derive an explicit closed-form profile for the induced negative energy density, and connect it to semiclassical backreaction.

A. Smeared Stress–Energy Operators and Operational Profiles

Following Ford and Roman [10, 11] and Fewster [8], we regulate the renormalized stress–energy density operator $\hat{T}_{00}(x)$ by convolution with a smooth, normalized sampling function. This

procedure is necessary because $\hat{T}_{00}(x)$, defined pointwise as in Eq. (A.6), suffers from ultraviolet divergences and requires smearing to yield finite expectation values.

To model a realistic measurement localized around the B–site at $\vec{x}_B$, we employ a Gaussian window of width σ:

$$f_\sigma(\vec{x}-\vec{x}_B) = \frac{1}{(\sqrt{\pi}\sigma)^3}\exp\Big(-\tfrac{|\vec{x}-\vec{x}_B|^2}{\sigma^2}\Big), \qquad \int d^3x\, f_\sigma(\vec{x}-\vec{x}_B) = 1. \tag{A.1}$$

The corresponding smeared energy density operator is then

$$\hat{T}_{00}^{(\sigma)}(t;\vec{x}_B) = \int d^3x\; f_\sigma(\vec{x}-\vec{x}_B)\,\hat{T}_{00}(t,\vec{x}). \tag{A.2}$$

This smearing procedure has a dual interpretation. On the one hand, it renders the operator mathematically well-defined by averaging over short-distance fluctuations. On the other hand, it models the finite spatial resolution of any realistic detector. As emphasized in Fewster [8], the smeared operator $\hat{T}_{00}^{(\sigma)}$ is therefore not an auxiliary object but the operationally measurable quantity.

In what follows, we use $\hat{T}_{00}^{(\sigma)}$ as the local probe of the perturbations generated by quantum energy teleportation (QET) protocols. This makes explicit that the stress–energy perturbations discussed later are already regulated in an experimentally meaningful way.

B. Hotta Protocol and Spatiotemporal Gaussian Energy Profiles

Following Hotta's quantum energy teleportation (QET) framework [14, 17], the B-site performs a local operation $\hat{U}_B(m) = \exp(i\epsilon_m \hat{O}_B)$ conditioned on outcome m of Alice's measurement. Here $\hat{O}_B$ is a localized field observable supported within the B region. Writing the B-Hamiltonian as

$$\hat{H}_B = \int d^3x\, w_B(\vec{x})\,\hat{T}_{00}(t_B,\vec{x}), \tag{A.3}$$

with a compactly supported weight w_B, the change in the B-energy conditioned on m is, to second order in ϵ_m,

$$\Delta E_B(m) = \epsilon_m\, C_m - \tfrac{1}{2}\,\epsilon_m^2\,\chi_B + \mathcal{O}(\epsilon_m^3), \tag{A.4}$$

where $C_m \equiv i\,\langle[\hat{O}_B,\hat{H}_B]\rangle_m$ and $\chi_B \equiv \langle[\hat{O}_B,[\hat{H}_B,\hat{O}_B]]\rangle_m \geq 0$.

From this expansion, the optimally extracted negative energy for outcome m is

$$\Delta E_B^*(m) = -\frac{C_m^2}{2\,\chi_B}. \tag{A.5}$$

This relation follows from the Baker–Campbell–Hausdorff expansion applied to $\hat{U}_B(m)^\dagger \hat{H}_B \hat{U}_B(m)$, truncated to $\mathcal{O}(\epsilon_m^2)$ [14].

To give this energy shift a local operational meaning, we connect it to the renormalized stress–energy tensor. Following Ford and Roman [10, 11, 8], the energy density operator is

$$\hat{T}_{00}(x) \;=\; \tfrac{1}{2}\big[(\partial_t\hat{\phi}(x))^2 + (\nabla\hat{\phi}(x))^2\big]_{\rm ren}. \tag{A.6}$$

Here "ren" denotes normal ordering or point-splitting subtraction relative to the Minkowski vacuum, ensuring $\langle 0|\hat{T}_{00}(x)|0\rangle = 0$.‡

To model locality, we smear with a normalized Gaussian window of spatial width σ around the B-site location $\vec{x}_B$:

$$f_\sigma(\vec{x}-\vec{x}_B) = \frac{1}{(\sqrt{\pi}\sigma)^3}\exp\Big(-\tfrac{|\vec{x}-\vec{x}_B|^2}{\sigma^2}\Big), \qquad \int d^3x\, f_\sigma(\vec{x}-\vec{x}_B) = 1, \tag{A.7}$$

and define the smeared operator

$$\hat{T}_{00}^{(\sigma)}(t;\vec{x}_B) = \int d^3x\ f_\sigma(\vec{x}-\vec{x}_B)\,\hat{T}_{00}(t,\vec{x}). \tag{A.8}$$

This smearing has two roles: (i) it regulates UV divergences by averaging over a finite spatial width, and (ii) it defines the operational profile of the energy density accessible to a detector localized in region B. Such Gaussian smearing functions are standard in quantum energy inequality (QEI) analyses [8].

The induced local perturbation from Bob's operation can then be modeled as

$$\delta\langle T_{00}(t_B,\vec{x})\rangle_m \ \equiv\ \langle T_{00}(t_B,\vec{x})\rangle_m - \langle T_{00}(t_B,\vec{x})\rangle_{\rm vac} = -A_m\, f_\sigma(\vec{x}-\vec{x}_B). \tag{A.9}$$

Integrating over all space,

$$\Delta E_B^*(m) = \int d^3x\,\delta\langle T_{00}(t_B,\vec{x})\rangle_m = -A_m\int d^3x\, f_\sigma(\vec{x}-\vec{x}_B) = -A_m, \tag{A.10}$$

so that

$$A_m \ =\ \Big|\Delta E_B^*(m)\Big| \ =\ \frac{C_m^2}{2\,\chi_B}. \tag{A.11}$$

Thus the Gaussian profile directly encodes the optimally extractable negative energy. In expectation over outcomes,

$$\delta\langle T_{00}(t_B,\vec{x})\rangle = -A\,\frac{1}{(\sqrt{\pi}\sigma)^3}\exp\Big(-\tfrac{|\vec{x}-\vec{x}_B|^2}{\sigma^2}\Big), \qquad A = \Big|\langle\Delta E_B\rangle\Big|. \tag{A.12}$$

In one spatial dimension (useful for waveguide or cavity line models) the corresponding normalized profile is

$$\delta\langle T_{00}(t_B,x)\rangle = -A\,\frac{1}{\sqrt{\pi}\sigma}\exp\Big(-\tfrac{(x-x_B)^2}{\sigma^2}\Big), \qquad \int dx\,\delta\langle T_{00}\rangle = -A. \tag{A.13}$$

Finally, temporal resolution can be incorporated by extending the smearing to a spatiotemporal Gaussian,

$$g_{\sigma,\tau}(t-t_B,\vec{x}-\vec{x}_B) = \frac{1}{\sqrt{\pi}\tau}\,e^{-(t-t_B)^2/\tau^2}\ \frac{1}{(\sqrt{\pi}\sigma)^3}\,e^{-|\vec{x}-\vec{x}_B|^2/\sigma^2}, \tag{A.14}$$

ensuring both spatial and temporal localization. This refinement is standard in QEI analyses, where temporally compact sampling functions are required for rigorous bounds [8].

‡ This renormalization removes the divergent zero-point energy. See Ford & Roman [11] and Fewster [8] for rigorous formulations of renormalized stress–energy in QFT.

C. Temporal Resolution and Spatiotemporal Gaussian Sampling

If the operation at B is temporally localized with a Gaussian of width τ centered at t_B, the fully smeared profile becomes

$$\delta\langle T_{00}(t,\vec{x})\rangle = -A\, g_\tau(t-t_B)\, f_\sigma(\vec{x}-\vec{x}_B), \quad g_\tau(t) = \frac{1}{\sqrt{\pi}\tau}\exp\Big(-\tfrac{t^2}{\tau^2}\Big), \tag{A.15}$$

so that $\int dt\, d^3x\, \delta\langle T_{00}\rangle = -A$. The limits $\tau \to 0$ or $\sigma \to 0$ are controlled by QEIs, as discussed next.

D. Quantum Energy Inequalities and Bounds on the Amplitude

Quantum energy inequalities bound the degree to which negative energy densities can be localized. For a broad class of sampling functions $g_\tau(t)$ (including Gaussians) and for free fields in Minkowski space, Fewster-type bounds imply

$$\int dt\, g_\tau^2(t)\, \langle T_{00}(t,\vec{x}_B)\rangle \;\geq\; -\frac{\kappa}{\tau^{d+1}}, \tag{A.16}$$

where d is the number of spatial dimensions (here $d=3$) and κ is a positive constant depending on the field content and the precise sampling choice [11, 8]. Combining Eq. (A.15) with Eq. (A.16) yields a constraint on the product of amplitude and localization widths. For separable Gaussian sampling one finds, schematically,

$$A \;\lesssim\; \frac{\kappa'}{\tau^{d+1}} \quad \text{and} \quad A \;\lesssim\; \frac{\tilde{\kappa}}{\sigma^{d+1}}, \tag{A.17}$$

where $\kappa', \tilde{\kappa}$ are order-unity constants set by the field and normalization conventions. Thus sharper localization (smaller σ or τ) forces a smaller allowed amplitude A, reflecting the tradeoff mandated by QEIs.

E. Semiclassical Backreaction and Summary

The smeared expectation value of the stress–energy perturbation produced by a localized QUINT/QET operation sources a small curvature response via the linearized semiclassical Einstein equation,

$$\delta G_{\mu\nu}(x) \;=\; 8\pi G\, \delta\langle \hat{T}_{\mu\nu}(x)\rangle, \tag{A.18}$$

where $\delta\langle \hat{T}_{\mu\nu}(x)\rangle$ is the renormalized, spatiotemporally smeared profile introduced in Eq. (A.15). Working to leading order in G (weak-field limit) the induced metric and curvature perturbations, $\delta g_{\mu\nu}$ and δR, are linear functionals of the smeared source and therefore inherit its Gaussian support and characteristic scales (σ, τ).

Observable signatures — interferometric phase shifts, small inertial forces, and clock-drift signals discussed in Sec. IV — scale linearly with the extracted-amplitude parameter

$$A \;=\; \Big|\langle \Delta E_B\rangle\Big| \tag{A.19}$$

appearing in Eq. (A.12).

In practice the linearized approximation is valid provided the dimensionless backreaction parameter

$$\varepsilon_{\rm GR} \;\sim\; \frac{G\,A}{\sigma^{\,d-1}} \tag{A.20}$$

remains $\ll 1$, so that higher-order gravitational corrections and nonperturbative effects can be neglected.

Crucially, the allowed amplitude A is not arbitrary: quantum energy inequalities (QEIs) constrain how sharply negative energy may be localized in space and time. For separable Gaussian sampling one finds the schematic bounds

$$A \;\lesssim\; \frac{\kappa'}{\tau^{\,d+1}}, \qquad A \;\lesssim\; \frac{\tilde{\kappa}}{\sigma^{\,d+1}}, \tag{A.21}$$

which enforce a tradeoff between localization and magnitude. These QEI limits therefore cap the maximum semiclassical curvature perturbation attainable from a single extraction event and, by linearity, constrain the cumulative signals from arrays of extractions.

In summary, the Hotta optimization fixes the *integrated* extractable energy $\langle \Delta E_B \rangle$, the smearing procedure furnishes an operational spatiotemporal profile for the induced $\delta\langle \hat{T}_{\mu\nu} \rangle$, and Eqs. (A.12)–(A.15) provide closed-form templates used in our figures. The resulting observable effects scale linearly with A but are ultimately bounded by QEIs (Eq. (A.25)) and by the requirement that gravitational backreaction remain perturbative (small $\varepsilon_{\rm GR}$), ensuring consistency with relativistic quantum field theory and semiclassical gravity.

F. Semiclassical Backreaction and Summary

The smeared expectation value of the stress–energy perturbation produced by a localized QUINT/QET operation sources a small curvature response via the linearized semiclassical Einstein equation,

$$\delta G_{\mu\nu}(x) \;=\; 8\pi G\,\delta\langle \hat{T}_{\mu\nu}(x) \rangle, \tag{A.22}$$

where $\delta\langle \hat{T}_{\mu\nu}(x) \rangle$ is the renormalized, spatiotemporally smeared profile introduced in Eq. (A.15). Working to leading order in G (weak-field limit) the induced metric and curvature perturbations, $\delta g_{\mu\nu}$ and δR, are linear functionals of the smeared source and therefore inherit its Gaussian support and characteristic scales (σ, τ).

Observable signatures — interferometric phase shifts, small inertial forces, and clock-drift signals discussed in Sec. IV — scale linearly with the extracted-amplitude parameter

$$A \;=\; \Big| \langle \Delta E_B \rangle \Big| \tag{A.23}$$

appearing in Eq. (A.12).

In practice the linearized approximation is valid provided the dimensionless backreaction parameter

$$\varepsilon_{\rm GR} \;\sim\; \frac{G\,A}{\sigma^{\,d-1}} \tag{A.24}$$

remains $\ll 1$, so that higher-order gravitational corrections and nonperturbative effects can be neglected.

Crucially, the allowed amplitude A is not arbitrary: quantum energy inequalities (QEIs) constrain how sharply negative energy may be localized in space and time. For separable Gaussian sampling one finds the schematic bounds

$$A \lesssim \frac{\kappa'}{\tau^{\,d+1}}, \qquad A \lesssim \frac{\tilde{\kappa}}{\sigma^{\,d+1}}, \tag{A.25}$$

which enforce a tradeoff between localization and magnitude. These QEI limits therefore cap the maximum semiclassical curvature perturbation attainable from a single extraction event and, by linearity, constrain the cumulative signals from arrays of extractions.

In summary, the Hotta optimization fixes the *integrated* extractable energy $\langle \Delta E_B \rangle$, the smearing procedure furnishes an operational spatiotemporal profile for the induced $\delta\langle \hat{T}_{\mu\nu} \rangle$, and Eqs. (A.12)–(A.15) provide closed-form templates used in our figures. The resulting observable effects scale linearly with A but are ultimately bounded by QEIs (Eq. (A.25)) and by the requirement that gravitational backreaction remain perturbative (small $\varepsilon_{\rm GR}$), ensuring consistency with relativistic quantum field theory and semiclassical gravity.

Appendix B. Discrete Update Model for Resource Evolution

To describe the dynamics of the shared entanglement resource during repeated QET cycles, we adopt a discrete-time update model. After each cycle, the effective resource amplitude R_n evolves according to the exact nonlinear update

$$R_{n+1} = R_\infty + (R_n - R_\infty)\, \exp(-\Delta t/\tau) - E_c, \tag{B.1}$$

where E_c is the extraction cost per cycle, τ is the recovery timescale, and R_∞ is the long-time equilibrium resource. Linearizing for $\Delta t \ll \tau$ gives

$$R_{n+1} \approx R_n - E_c + \frac{\tau - \Delta t}{\tau}(R_\infty - R_n), \tag{B.2}$$

Stability of this fixed point can be analyzed by defining the deviation $\delta_n \equiv R_n - R^*$. From Eq. (B.2), one finds

$$\delta_{n+1} = \frac{\Delta t}{\tau}\, \delta_n. \tag{B.3}$$

Thus, the fixed point is stable if and only if

$$\left| \frac{\Delta t}{\tau} \right| < 1 \quad \Longleftrightarrow \quad 0 < \Delta t < \tau, \tag{B.4}$$

Physical feasibility requires a non-negative steady-state resource, $R^* \geq 0$, which leads to the constraint

$$R_\infty - \frac{\tau}{\Delta t}\, E_c \geq 0 \quad \Longleftrightarrow \quad E_c \leq \frac{\Delta t}{\tau} R_\infty. \tag{B.5}$$

Operationally, one can distinguish several regimes. In the slow-cycle regime ($\Delta t \ll \tau$), convergence to $R^* \approx R_\infty - (\tau/\Delta t)E_c$ is rapid, and E_c must scale down with Δt to maintain

$R^* > 0$. For marginal cycles ($\Delta t \lesssim \tau$), convergence is slow and the feasibility bound is the tightest. If extraction is too fast (large E_c at fixed Δt), the feasibility condition is violated, leading to progressive depletion toward zero.

The idealized power per cycle is given by

$$P = \frac{E_c}{\Delta t}, \qquad P_{\max} \leq \frac{R_\infty}{\tau}, \tag{B.6}$$

with the maximum constrained by the resource recovery rate. The closed-form trajectory of the recursion can be written as

$$R_n = R^* + \left(\frac{\Delta t}{\tau}\right)^n (R_0 - R^*), \tag{B.7}$$

showing that deviations decay geometrically. The number of cycles required to reach a tolerance ε is

$$n_\varepsilon \approx \frac{\ln(\varepsilon/|R_0 - R^*|)}{\ln(\Delta t/\tau)}, \quad 0 < \Delta t/\tau < 1. \tag{B.8}$$

Equation (B.2) expresses the balance between depletion by extraction (E_c) and recovery toward R_∞. The contraction factor $\Delta t/\tau$ governs both the stability of the fixed point and the rate of convergence toward it.

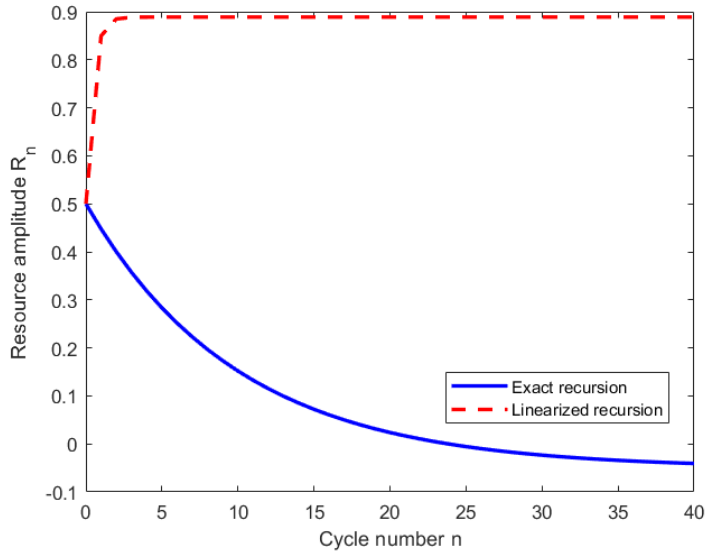

Figure B1: Illustration of the discrete update dynamics given by Eq. (B.1). Solid line: exact nonlinear recursion. Dashed line: linearized approximation (B.2). Parameters chosen for clarity: $\tau = 10$, $\Delta t = 1$, $E_c = 0.1$, $R_\infty = 1$.

Appendix C. Bessel/Interference Structure, Angular Harmonics, and Nodes

A. Origin of nodes in $\Gamma(N, d)$

The network enhancement factor $\Gamma(N, d)$ captures interference between stress–energy deficit profiles generated at different nodes. At leading order, it can be expressed in a pairwise form,

$$\Gamma(N, d) \;\approx\; 1 + \frac{1}{N} \sum_{i \neq j} \mathcal{I}(d_{ij}), \tag{C.1}$$

where $d_{ij} = |\mathbf{d}_{ij}|$, and $\mathcal{I}(d)$ is the normalized cross-overlap of the induced deficits,

$$\mathcal{I}(d) \;=\; \frac{\displaystyle\int d^3x\, \delta T_i^{00}(\mathbf{x})\, \delta T_j^{00}(\mathbf{x} + \mathbf{d})}{\displaystyle\int d^3x\, \delta T_i^{00}(\mathbf{x})\, \delta T_j^{00}(\mathbf{x})}. \tag{C.2}$$

For cylindrically or spherically symmetric propagation with a dominant wavenumber k and finite correlation length λ, the overlap acquires an oscillatory-decaying form. Using a consistent zeroth-order Bessel function notation J_0,

$$\mathcal{I}(d) \;\simeq\; J_0(kd)\, e^{-d/\lambda} \;=\; \frac{\sin(kd)}{kd}\, e^{-d/\lambda}. \tag{C.3}$$

This arises from the angular integral in the continuum limit,

$$\int_0^{2\pi} e^{ikr\cos\theta}\, d\theta \;=\; 2\pi J_0(kr), \tag{C.4}$$

Nodes (zeros or minima) in Γ therefore occur approximately at $kd \approx n\pi$, where n is an integer. Equation (C.3) provides the radial analogue of the angular lobes, and represents the continuum limit of the pairwise phase factors appearing in discrete arrays (cf. lattice sums of $e^{i\mathbf{k}\cdot\mathbf{d}_{ij}}$).

subsectionAngular harmonics and physically motivated toy models The polar "toy" patterns used in Sec. V represent simplified angular kernels $\mathcal{A}(\hat{\mathbf{d}})$ for studying interference in node arrays. Three common models are considered:

Model 1 uses a quadrupole-like pattern, $\mathcal{A}(\hat{\mathbf{d}}) = |\cos 2\theta|^p$. This model captures strong directional selectivity along principal axes and is useful for illustrating sharp lobe structures in small arrays. Its strength lies in providing clear visual intuition for angular nodes and the influence of lobe sharpness p on the interference pattern.

Model 2 employs a weakly modulated cosine, $\mathcal{A}(\hat{\mathbf{d}}) = 1 + \varepsilon\cos(m\theta)$. This model is smoother and accommodates more flexible symmetries (m-fold) while maintaining modest anisotropy. Its strength is in representing physically realistic arrays where elements are not perfectly aligned and the angular dependence is subtle.

Model 3 combines a Gaussian envelope with mild angular modulation, $\mathcal{A}(\hat{\mathbf{d}}) = e^{-\rho^2 \sin^2\theta}(1 + B\cos 2\theta)$. This captures both the directional selectivity and finite angular spread of real wave packets. Its strength is in approximating realistic decoherence or beam-width effects, providing a more physically accurate representation of the angular coupling between array elements.

Each of these models can be combined with a radial kernel $\mathcal{R}(d) \approx j_0(kd)\, e^{-d/\lambda}$ to generate the full lattice sum $\Gamma(N, d)$ in Eq. (C.5), and to explore the combined effects of angular and radial interference in the array.

B. Linking angular nodes to $\Gamma(N, d)$

The angular lobes (Models 1–3) and the radial nodes in (C.3) represent two complementary facets of the same interference physics. Angular selection rules such as $\cos 2\theta$ or more general $\cos m\theta$ dependencies govern the *directional* coupling strengths between elements in an array, while radial interference governed by $j_0(kd)$ determines the *range*, producing node lines in (N, d) slices as illustrated in Fig. 5. In discrete arrays these two effects combine naturally as lattice sums of the form

$$\Gamma(N,d) \;\sim\; 1+\frac{1}{N}\sum_{i\neq j}\Big[\mathcal{A}(\hat{\mathbf{d}}_{ij})\,\mathcal{R}(d_{ij})\Big], \qquad \mathcal{A}(\hat{\mathbf{d}}) \in \{\,|\cos 2\theta|^{p},\; 1+\varepsilon\cos(m\theta),\; e^{-\rho^2\sin^2\theta}(1+B\cos 2\theta)\,\}, \tag{C.5}$$

with $\mathcal{R}(d) \approx j_0(kd)\, e^{-d/\lambda}$ as in (C.3). Angular nodes arising from $\mathcal{A}$ and radial nodes arising from $\mathcal{R}$ together account for the lobe and ridge structure observed in the heat map.

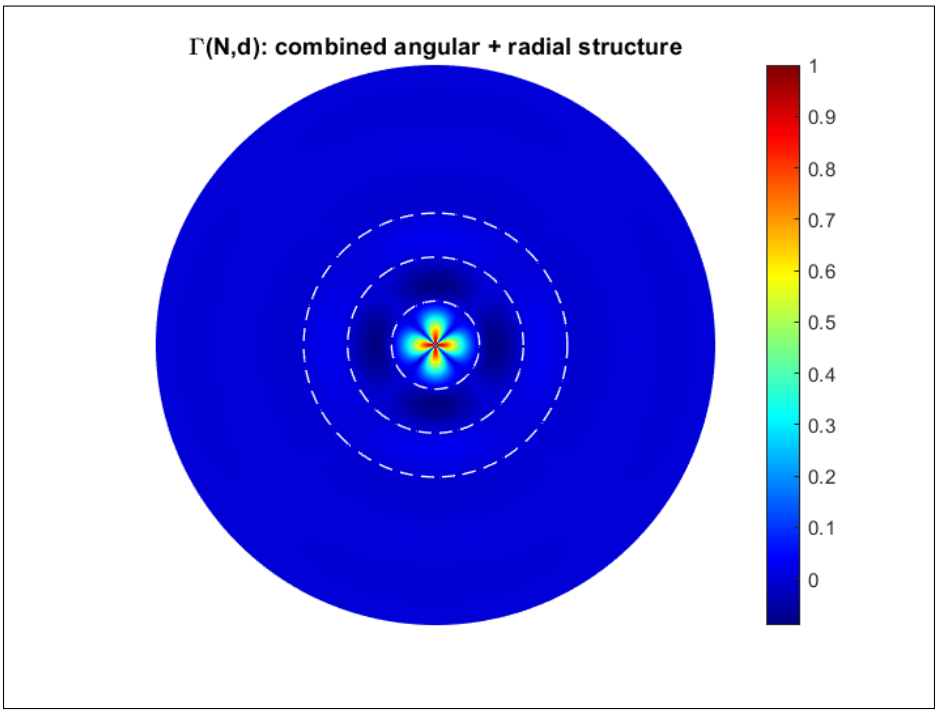

Figure C1: Combined angular and radial interference structure for the network enhancement factor $\Gamma(N, d)$ (Eq. (C.5)). The colormap shows the amplitude resulting from the product of an angular toy model (e.g., quadrupole $|\cos 2\theta|$) and a radial Bessel-like kernel $j_0(kd)\, e^{-d/\lambda}$. White dashed circles indicate the first few zeros of $j_0(kd)$, highlighting radial nodes in the array. This figure illustrates how directional angular lobes and radial interference jointly produce the lobe/ridge patterns seen in heat maps of $\Gamma(N, d)$.

C. Practical parameter ties

For plotting and fitting, the quadrupole model is characterized by the parameters p (sharpness), A (anisotropy), and r_0 (baseline). The Gaussian overlap model introduces $\rho = d/(2w)$, a measure

of the ratio of separation to mode waist, along with B (weak anisotropy) and r_0. The corrugation model depends on m (symmetry), ε (contrast), and r_0. Finally, the radial kernel involves the effective band-center k and the correlation length λ. In simulations, (k, λ) can be tied to detector bandwidth and environmental cutoffs, (m, ε) to patterned boundaries, and ρ to the waist-to-separation ratio.

Remark. Minor deviations from exact j_0 behavior, such as the presence of multiple bands or weak dissipation, can be modeled by replacing $j_0(kd)$ with a short weighted sum $\sum_\alpha w_\alpha j_0(k_\alpha d)$ and adjusting the decay envelope to a stretched exponential $e^{-(d/\lambda)^\nu}$ with $1 \leq \nu \leq 2$.

References

[1] B. P. Abbott *et al.* (LIGO Scientific Collaboration and Virgo Collaboration), "Observation of Gravitational Waves from a Binary Black Hole Merger," *Phys. Rev. Lett.* **116**, 061102 (2016).

[2] M. Alcubierre, "The warp drive: hyper-fast travel within general relativity," *Class. Quantum Grav.* **11**, L73 (1994).

[3] C. H. Bennett, G. Brassard, C. Crépeau, R. Jozsa, A. Peres, and W. K. Wootters, "Teleporting an Unknown Quantum State via Dual Classical and Einstein-Podolsky-Rosen Channels," *Phys. Rev. Lett.* **70**, 1895–1899 (1993).

[4] A. S. Cacciapuoti, C. Pellitteri, J. Illiano, L. d'Avossa, F. Mazza, S. Chen, and M. Caleffi, "Quantum Data Centers: Why Entanglement Changes Everything," *arXiv preprint arXiv:2506.02920*, 2025.

[5] H. B. G. Casimir, "On the Attraction Between Two Perfectly Conducting Plates," *Proc. K. Ned. Akad. Wet.* **51**, 793–795 (1948).

[6] C.-H. Chou, T. Yu, and B. L. Hu, "Entanglement dynamics in open quantum systems: Theoretical aspects," *Phys. Rev. E* **77**, 011112 (2008).

[7] J. I. Cirac, P. Zoller, H. J. Kimble, and H. Mabuchi, "Quantum State Transfer and Entanglement Distribution among Distant Nodes in a Quantum Network," *Phys. Rev. Lett.* **78**, 3221–3224 (1997).

[8] C. J. Fewster, "Energy inequalities in quantum field theory," in *XVIth International Congress on Mathematical Physics*, edited by P. Exner (World Scientific, Singapore, 2005), pp. 163–173. [arXiv:math-ph/0501073].

[9] L. H. Ford and T. A. Roman, "Averaged energy conditions and quantum inequalities," *Phys. Rev. D* **51**, 4277–4286 (1995).

[10] L. H. Ford, "Quantum field theory in curved spacetime," in *100 Years of Relativity: Spacetime Structure—Einstein and Beyond*, edited by A. Ashtekar, (World Scientific, Singapore, 2005), pp. 293–310. [Originally based on lectures from 1996]. arXiv:gr-qc/9604002

[11] L. H. Ford and T. A. Roman, "Restrictions on negative energy density in flat spacetime," *Phys. Rev. D* **55**, 2082 (1997).

[12] L. H. Ford, "Spacetime metrics and quantum inequalities," *Int. J. Mod. Phys. A* **14**, 146–163 (1999). doi:10.1142/S0217751X9900005X

[13] L. H. Ford and T. A. Roman, "Restrictions on negative energy density in flat spacetime," *Phys. Rev. D* **62**, 105011 (2000).

[14] M. Hotta, "Quantum energy teleportation with electromagnetic field: Discrete-variable protocol," *Phys. Lett. A* **372**, 5671–5676 (2008).

[15] M. Hotta, "Quantum energy teleportation in spin chain systems," *Phys. Rev. A* **78**, 042311 (2008). doi:10.1103/PhysRevA.78.042311

[16] M. Hotta, "Quantum energy teleportation with trapped ions," *Phys. Lett. A* **372**, 5671–5676 (2008). doi:10.1016/j.physleta.2008.07.061

[17] M. Hotta, "Quantum energy teleportation with electromagnetic field: Discrete vs. continuous-variable protocols," *Phys. Rev. D* **79**, 045006 (2009).

[18] M. Hotta, "Energy entanglement in quantum field theory and the extraction of zero-point energy," *Phys. Rev. D* **78**, 045006 (2008).

[19] M. Hotta, "Quantum energy teleportation in spin chain systems," *Phys. Rev. A* **83**, 062323 (2011).

[20] M. Hotta, R. Schützhold, and W. G. Unruh, "Partner particles for moving mirror radiation and black hole evaporation," *Phys. Rev. D* **91**, 124060 (2015).

[21] H. J. Kimble, "The Quantum Internet," *Nature* **453**, 1023–1030 (2008).

[22] P. W. Milonni, *The Quantum Vacuum: An Introduction to Quantum Electrodynamics* (Academic Press, San Diego, 1994).

[23] J. Preskill, "Challenges at the entanglement frontier," 2019, `https://www.orau.gov/qispi2018/plenary/Preskill_Plenary_QIS_Meeting_2019.pdf`.

[24] A. Reiserer, "Cavity-enhanced quantum network nodes," *Reviews of Modern Physics*, vol. 94, no. 4, p. 041003, 2022.

[25] B. Swingle and M. Van Raamsdonk, "Universality of gravity from entanglement," arXiv:1405.2933 [hep-th] (2014).

[26] M. Van Raamsdonk, "Building up spacetime with quantum entanglement," *Gen. Relativ. Gravit.* **42**, 2323–2329 (2010).

[27] A. Wallraff, D. I. Schuster, A. Blais, L. Frunzio, R.-S. Huang, J. Majer, S. Kumar, S. M. Girvin, and R. J. Schoelkopf, "Strong Coupling of a Single Photon to a Superconducting Qubit Using Circuit Quantum Electrodynamics," *Nature* **431**, 162–167 (2004).

[28] D. J. Wineland, "Nobel Lecture: Superposition, Entanglement, and Raising Schrödinger's Cat," *Rev. Mod. Phys.* **85**, 1103–1114 (2013).

[29] K. Yamamoto, "Implementation of quantum energy teleportation in harmonic oscillator systems," *Phys. Rev. A* **92**, 042316 (2015).

[30] OpenAI, "ChatGPT (June 2025 version)," `https://chat.openai.com`, accessed June 2025.

[31] OpenAI, "GPT-4 Technical Report," arXiv:2303.08774 (2023), arXiv:2303.08774.